energies

MDPI

Article

Investigations of Flow and Heat Transfer Characteristics in a Channel Impingement Cooling Configuration with a Single Row of Water Jets

Min-Seob Shin, Santhosh Senguttuvan and Sung-Min Kim *

School of Mechanical Engineering, Sungkyunkwan University, 300 Cheoncheon-dong, Suwon 16419, Korea; msky1128@skku.edu (M.-S.S.); santhosh@skku.edu (S.S.)
* Correspondence: smkim@skku.edu; Tel.: +82-31-290-7433

Abstract: The present study experimentally and numerically investigates the effect of channel height on the flow and heat transfer characteristics of a channel impingement cooling configuration for various jet Reynolds numbers in the range of 2000–8600. A single array consisting of eleven jets with 0.8 mm diameter injects water into the channel with 2 mm width at four different channel heights (3, 4, 5, and 6 mm). The average heat transfer coefficients at the target surface are measured by maintaining a temperature difference between the jet exit and the target surface in the range of 15–17 °C for each channel height. The experimental results show the average heat transfer coefficient at the target surface increases with the jet Reynolds number and decreases with the channel height. An average Nusselt number correlation is developed based on 85 experimentally measured data points with a mean absolute error of less than 4.31%. The numerical simulation accurately predicts the overall heat transfer rate within 10% error. The numerical results are analyzed to investigate the flow structure and its effect on the local heat transfer characteristics. The present study advances the primary understanding of the flow and heat transfer characteristics of the channel impingement cooling configuration with liquid jets.

Keywords: jet impingement; confined array jets; heat transfer coefficient; computational fluid dynamics

check for updates

Citation: Shin, M.-S.; Senguttuvan, S.; Kim, S.-M. Investigations of Flow and Heat Transfer Characteristics in a Channel Impingement Cooling Configuration with a Single Row of Water Jets. *Energies* **2021**, *14*, 4327. https://doi.org/10.3390/en14144327

Academic Editor: Dimitris Drikakis

Received: 18 June 2021
Accepted: 14 July 2021
Published: 18 July 2021

Publisher's Note: MDPI stays neutral with regard to jurisdictional claims in published maps and institutional affiliations.

Copyright: © 2021 by the authors. Licensee MDPI, Basel, Switzerland. This article is an open access article distributed under the terms and conditions of the Creative Commons Attribution (CC BY) license (https://creativecommons.org/licenses/by/4.0/).

1. Introduction

High power density devices such as computer chips, power inverters, X-ray systems, and microwave weapons have been undergoing size miniaturization in the past decade, leading to increased demand for high heat flux removal from a small surface area. For the safe operation of the high-power density devices, maintaining constant and uniform temperature is an important task. Hence, different convection cooling schemes, including microchannel heat sink [1–4], spray cooling [5,6], and jet impingement [7–10], were developed to deal with the high heat flux.

Jet impingement cooling, ejecting high-velocity coolant from a nozzle or an orifice plate perpendicular to the target surface, yields a highly concentrated heat removal rate at the impact zone, which effectively cools a small area dissipating high heat flux. By utilizing both air and liquid as coolant, jet impingement cooling was studied in a variety of fields demanding dissipation of highly concentrated heat; cooling of blades in a gas turbine engine [11–20], quenching process in steel industries [21], and avionics cooling [22]. Jet impingement cooling is classified into three different configurations [23]: free jet when the jet is injected into less dense ambient fluid, submerged jet when the jet is injected into the same ambient fluid, and confined jet when the jet is injected into a confined space between the orifice plate and the target surface filled with the same fluid. In the confined jet configuration, the confined space forms a passage to guide the spent fluid towards the outlet, making it easier to extract the spent flow. When a jet impinges on the target surface,

two different flow regions develop near the surface, such as the stagnation and wall jet regions. In the stagnation region, the impinging flow changes its trajectory into radially accelerating outward flow due to pressure gradient, causing a high heat transfer rate because of boundary layer thinning. On the other hand, the radial flow decelerates at the wall jet region, and the heat transfer rate decreases along the radial direction. One drawback of jet impingement cooling is a high cooling rate difference between the stagnation and the wall jet regions, making a single jet inadequate for cooling a large surface area. However, this drawback can be overcome by using an array of jets to cover a large surface area, resulting in uniform temperature on the target surface. In the array configuration, the spent fluid ejected from the upstream jet forms a crossflow. The crossflow deflects the trajectories of the downstream jets, which impinges on the target surface at an angle. Several studies [24–26] reported that the crossflow has a detrimental effect on the heat transfer rate at the target surface.

Numerous studies were conducted to reduce the effect of crossflow in an array jet configuration. A hybrid impingement/effusion cooling scheme has been implemented for turbine blade cooling [12–15]. In the hybrid impingement/effusion cooling scheme, the spent fluid is extracted to effusion holes on the target surface or jet orifice plate, significantly reducing crossflow. Hollworth et al. [12] investigated the heat transfer of an array jet impingement cooling with effusion holes at the target surface. They compared their results with the cases without effusion holes and found that the array jet with effusion holes had a 20–30% higher heat transfer rate. Huber and Viskanta [13] investigated an array jet impingement cooling scheme in which both jet holes and effusion holes were on the orifice plate. They found that the existence of effusion holes reduces crossflow and interference between jets, greatly enhancing heat transfer rate. Zhang et al. [15] compared the cooling performance of the hybrid impingement/effusion cooling and effusion cooling of a multi swirler combustor. They also concluded that the hybrid impingement/effusion cooling method was highly effective. A similar concept of extracting spent fluids was widely investigated in electronics cooling [7–10]. Natarazan and Bezama [7] experimentally examined a micro-jet array cooler manufactured with multilayer ceramic technology for thermal management of high-power dissipating electronic chips, which includes an array of spent fluid extraction holes between jet holes. They achieved more than 250 W/cm^2 of heat dissipation with a pressure drop of less than 70 kPa. Wu et al. [10] investigated an array jet impingement cooling for a simulated chip using an additively manufactured manifold design that encloses the chip with working fluid. They fabricated an array of extraction holes between adjacent jet holes to prevent the crossflow formation and jet interference between neighboring jets in their design. In summary, extracting spent flow improves heat transfer performance in array jet cooling. The main drawbacks are the complicated plenum design and difficulties in fabrication.

On the contrary, several studies have utilized crossflow to enhance the heat transfer by using a narrow channel configuration. Channel impingement cooling scheme was investigated for cooling turbine blade leading edge [16–19]. In this configuration, single or double rows of jets impinge on the target surface, and the crossflow is guided along the channel formed by the target surface, sidewall, and jet plate. Jet impingement at the target surface and crossflow inside the channel both contribute to heat transfer. The primary geometric parameters in this cooling scheme are jet hole diameter (D_{jet}), channel height (H_{ch}), channel width (W_{ch}), jet hole pitch (X_{jet}), and the number of jets (N_{jet}). Ricklick et al. [16] experimentally investigated the overall heat transfer of the channel impingement cooling scheme with a single row of jets at H_{ch}/D_{jet} = 1, 3, 5. They reported that significant heat transfer occurs at the sidewall of the channel, and it increases for smaller H_{ch} due to a higher crossflow rate. They also concluded that the channel impingement cooling scheme is an effective method with respect to coolant usage. Fechter et al. [17] performed an experimental and numerical study on a narrow channel consisting of a single row of jet holes with an inline and staggering arrangement. They reported overall heat transfer rate by both experiment and numerical prediction. Moreover, they found that mass flow rate

variation occurs between jet holes due to channel pressure drop. The numerical prediction was calculated using the Shear Stress Transport (SST) k-ω turbulence model, which agreed well with experimental results. Terzis et al. [18] experimentally investigated local heat transfer on the target plate, sidewalls, and jet plate for various X_{jet}, W_{ch}, H_{ch}, and jet offset conditions using transient liquid crystal technique. They developed a local heat transfer correlation at the target plate, sidewalls, and jet plate as a function of jet velocity, channel crossflow rate, and geometric parameters.

The channel impingement cooling concept can dissipate high heat flux from a small surface area using a liquid jet and a mini/micro-channel. By taking advantage of both micro-channel and jet impingement, a hybrid micro-channel/micro-circular-jet-impingement cooling method using dielectric fluid HFE-7100 was proposed by Sung and Mudawar [26]. They investigated the effect of micro-channel dimensions on the overall heat transfer characteristics of the hybrid cooling method. They showed that this cooling scheme combines the heat transfer characteristics of both micro-channel and jet impingement, and the effect of jet impingement cooling increased with increasing mass flow rate. Sung and Mudawar [27] studied the effect of jet patterns on the hybrid cooling method both experimentally and numerically. They also found that the contribution of jet impingement cooling on overall heat transfer increased with increasing mass flow rate. Further, they developed a single heat transfer coefficient correlation using the superpositioning technique, in which heat transfer at each portion of the heat transfer surface was assigned as jet impingement or channel cooling. Barrau et al. [28] experimentally investigated the hybrid jet impingement/micro-channel cooling scheme using water. Later, Barrau et al. [29] studied the hybrid jet impingement/micro-channel cooling scheme numerically and found that the SST k-ω turbulence model can effectively predict overall heat transfer characteristics. The channel impingement cooling scheme with liquid has the ability to dissipate high heat flux from a small surface; for example, Sung and Mudawar [30] were able to dissipate more than 300 W/cm^2 without phase change.

The local heat transfer at the target surface and the sidewalls were extensively studied in the channel impingement cooling scheme with air. However, most of the research in the channel impingement cooling scheme with liquid focuses primarily on the overall heat transfer [26–30]. Hence, it is essential to investigate the heat transfer at each surface in the channel impingement cooling scheme with liquid to understand the complex heat transfer mechanism comprehensively. For the channel impingement cooling with liquid to become a viable thermal management scheme, it is crucial to attaining an effective design tool, such as a heat transfer coefficient correlation at each surface [18] and a valid numerical model [17,29].

The objective of the present study is to investigate the heat transfer characteristics at the target surface and flow characteristics of channel impingement cooling with water as a working fluid at different channel heights. Eleven equally-spaced (X_{jet}/D_{jet} = 6) jet holes with D_{jet} = 0.8 mm supply deionized water to a narrow channel (W_{ch}/D_{jet} = 2.5) at four different channel heights (H_{ch} = 3, 4, 5, and 6 mm) and the spent water exits through both ends of the channel. The average heat transfer coefficients at the target surface are experimentally measured for jet Reynolds numbers (Re_{jet}) ranging from 2000 to 8600. A new correlation is developed for predicting the average Nusselt number at the target surface. Moreover, numerical simulations are performed to analyze the observed experimental trends and investigate the internal flow structure and heat transfer in the channel impingement configuration.

2. Experimental Method

2.1. Flow Loop

Figure 1 shows the closed circulation flow loop for supplying deionized water to a test module containing the channel impingement cooling configuration. An insertion heater in the water reservoir provides water at the desired temperature (30 °C) to the flow loop. A magnetic gear pump (DGS series, Tuthill, Burr Ridge, IL, USA) connected to an inverter is

used to pump water through the loop. The water is passed through a 45 µm inline filter before entering the test section. The total flow rate is monitored by a Coriolis mass flow meter (ALTI mass, Oval Corp., Tokyo, Japan) and is adjusted to obtain the desired value by controlling the needle valve. The spent water leaves the test module through two outlets. A rotameter is installed at one of the outlets to ensure equal flow rates at each outlet. The spent water rejects heat to an external water loop via a water-to-water heat exchanger and returns to the water reservoir. T-type thermocouples and pressure transducers (PX-409, Omega engineering, Norwalk, CT, USA) are connected to a data acquisition system to measure the flow conditions at the inlet and outlets of the test module.

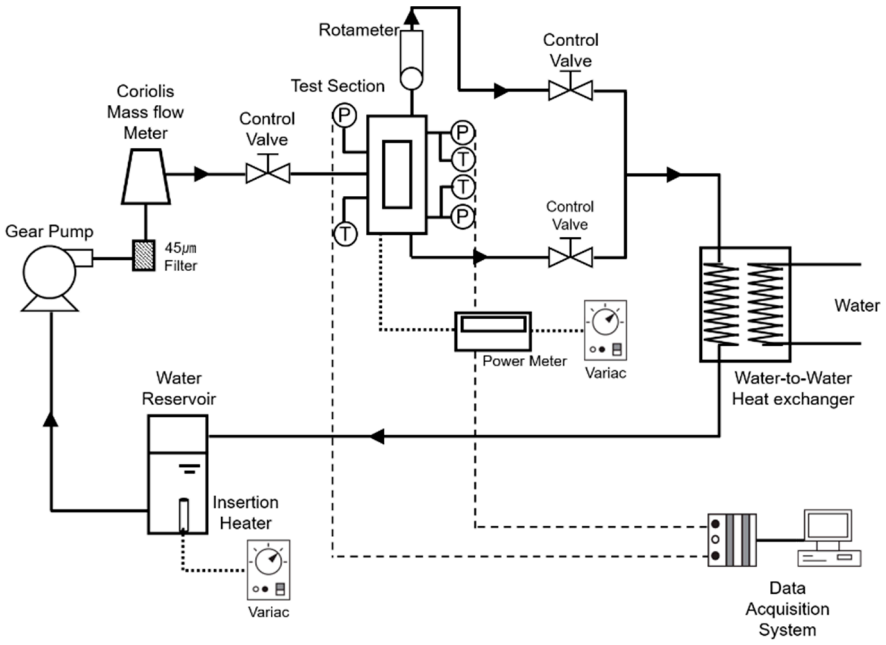

Figure 1. Schematic of flow loop.

2.2. Test Module

Figure 2 presents the exploded and sectional views of the test module. The test module has a layered structure composed of inlet housing, jet plate, channel plate, outlet housing, insulation housing, and copper heating block inserted with three cartridge heaters. The inlet housing is made of transparent polycarbonate to observe the water level in the inner inlet plenum. Thermocouples and pressure transducers are installed at the inlet plenum and both the outlets. Water supplied to the inlet plenum passes through orifice-type jet holes and impinges on the top surface of the heating block, which is flush-mounted into the middle of the outlet housing. The channel plate is machined to form a channel in the middle, which guides impinged water to the outlet plenum at both sides of the outlet housing. The channel plates are made of polycarbonate, which has low thermal conductivity (k_s = 0.2 W/m-K) to reduce heat transfer from the channel sidewalls and observe possible air bubbles inside the channel. Room-temperature-vulcanizing (RTV) silicone is applied at the contact region between the outlet housing and the copper heating block to prevent water leakage. The copper heating block is fabricated in a flange shape and held between the outlet housing and the insulation housing. Three holes are formed at the bottom of the heating block for cartridge heaters insertion. To prevent water leakage, Viton O-rings (Chemours, Wilmington, DE, USA) are inserted between each layer of the test module. To ensure O-rings are compressed evenly, the test module is compressed between 20 mm thick top and bottom stainless steel support frames.

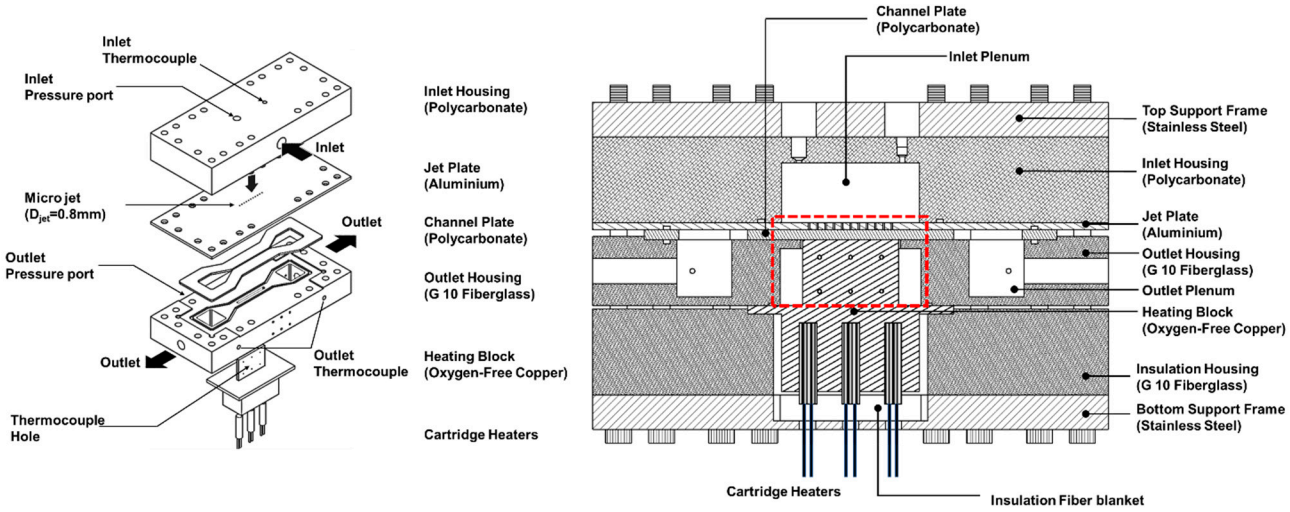

Figure 2. Exploded and sectional views of test module.

Figure 3 shows the schematic of the side and front views of the test section region (region marked by a red dashed line in Figure 2). A total of 11 jet holes with a diameter (D_{jet}) equal to 0.8 mm are drilled on the jet plate along the channel length. The thickness of the extruded part of the copper heating block (t_{copper}) is larger than the channel width (W_{ch}), and the wetted area is smaller than the target surface area. The heat flux (q'') through the heating block is calculated using Fourier's law.

$$q'' = k_{copper} \frac{T_{tc.2} - T_{tc.1}}{H_{tc.2}} \tag{1}$$

where $T_{tc.1}$ and $T_{tc.2}$ are the average temperatures, and $H_{tc,2}$ is the vertical distance between the locations of the thermocouples. $T_{tc.1}$ and $T_{tc.2}$ are given as,

$$T_{tc.1} = \frac{T_{tc.L1} + T_{tc.M1} + T_{tc.R1}}{3} \tag{2}$$

$$T_{tc.2} = \frac{T_{tc.L2} + T_{tc.M2} + T_{tc.R2}}{3} \tag{3}$$

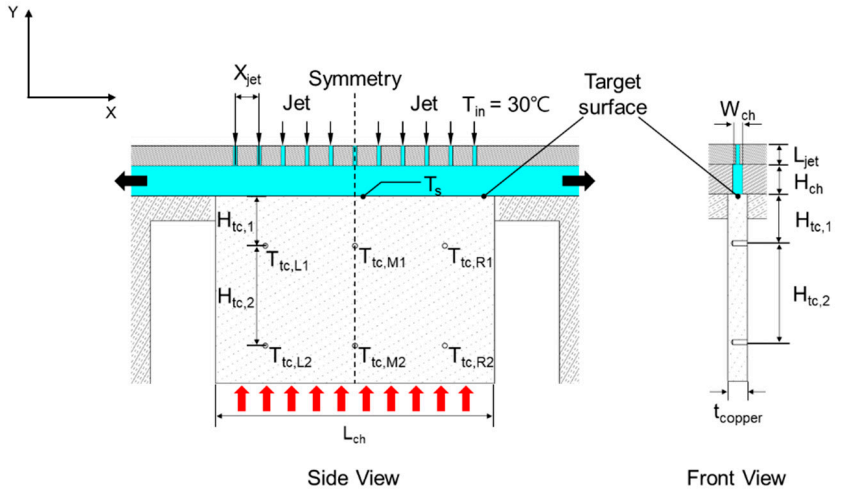

Figure 3. Schematic of side and cross-sectional views of test section.

Mean target surface temperature (T_s) is calculated by assuming a linear temperature profile in the upward direction using Equation (4).

$$T_s = T_{tc.1} + \frac{H_{tc,1} q''}{k_{copper}} \quad (4)$$

Since W_{ch} is smaller than t_{copper}, considering an energy balance between the wetted area and the target surface area, the area-averaged heat transfer coefficient at the target surface (h_{avg}) is calculated as follows:

$$h_{avg} = \frac{q''}{T_s - T_{in}} \frac{t_{copper}}{W_{ch}} \quad (5)$$

where T_{in} is the jet exit temperature. The detailed geometric dimensions of the test section are given in Table 1.

Table 1. Test section dimensions.

D_{jet} (mm)	X_{jet} (mm)	L_{jet} (mm)	N_{jet}	W_{ch} (mm)	H_{ch} (mm)	L_{ch} (mm)	t_{copper} (mm)	$H_{tc,1}$ (mm)	$H_{tc,2}$ (mm)
0.8	4.8	3	11	2	3, 4, 5, 6	56	4	8	22

2.3. Operating Procedure

Prior to the experiments, the pump was operated for a few hours to remove air that might be trapped inside the test module and the flow loop. More than 20 cases were tested for each channel height. The operating conditions are summarized in Table 2. The temperature difference between T_{in} and T_s was maintained between 15–17 °C throughout the experiments to exclude the natural convection effect. The steady-state was determined when temperature changes at the heating block and inlet plenum were smaller than 0.2 °C for over three minutes. Data including temperature, mass flow rate, and pressure were recorded for 5 min after the steady-state was achieved at each operating condition. The experiments were conducted in the order of highest average jet velocity (V_{jet}) to the lowest V_{jet} for each channel height (H_{ch}). After recording the data for each V_{jet}, the mass flow rate was adjusted to reduce V_{jet} by 0.2–0.3 m/s, and power input was reduced by 1–3 W. The same procedures are repeated until V_{jet} reached around 2 m/s.

Table 2. Experimental operating conditions.

H_{ch} (mm)	V_{jet} (m/s)	Re_{jet}	q'' (W/cm^2)	Number of Cases
3	2.00–8.27	2044–8475	13.2–35.4	22
4	1.98–8.35	2031–8552	14.7–30.5	21
5	2.00–8.31	2044–8509	13.9–29.7	21
6	2.00–8.28	2047–8478	12.2–26.4	21

2.4. Measurement Uncertainty

Maximum uncertainties in measuring absolute pressure and volume flow rate are 0.3% and 0.1%, respectively. T-type thermocouples used in the experiments are calibrated with an RTD sensor (PT 100 RTD, Omega engineering, Norwalk, CT, USA) which has ±0.1 °C uncertainty. Considering a conservative uncertainty of 2% in length measurement, maximum uncertainty in heat flux measurement is determined to 2.82% at minimum heat flux condition. The resultant maximum uncertainty in the heat transfer coefficient is determined as 9.32%.

3. Numerical Model

3.1. Model Description

Only one-quarter of the channel impingement cooling configuration was modeled considering the symmetry at $X = 0$ and $Z = 0$ planes, as shown in Figure 4a. Figure 4b illustrates the schematic of the numerical domain consisting of the extruded part of the copper heating block and the fluid region, including the inlet plenum. Mass flow inlet condition was specified at the inlet plenum, which provides distributed flow to each jet hole. To ensure that the backflow from the exit does not affect the heat transfer result, the fluid domain at the exit was extended. A constant wall heat flux condition was applied at the bottom of the heating block. Boundaries directly in contact with the polycarbonate channel plate were assumed as an adiabatic wall because the heat transfer from the polycarbonate channel plate to the fluid was calculated to be less than 3% of total heat input by numerical simulation, which included the polycarbonate material domain. Figure 4c shows the numerical grid generated in ICEM 19.1 (ANSYS Inc., Canonsburg, PA, USA) meshing module using a multi-block strategy. The numerical domain was discretized into hexahedral elements for the accuracy of numerical solutions. The first cell from the wall is located close to the wall to achieve a dimensionless wall distance ($y+$) value less than 1 for using the Shear Stress Transport (SST) k-ω turbulence model [31].

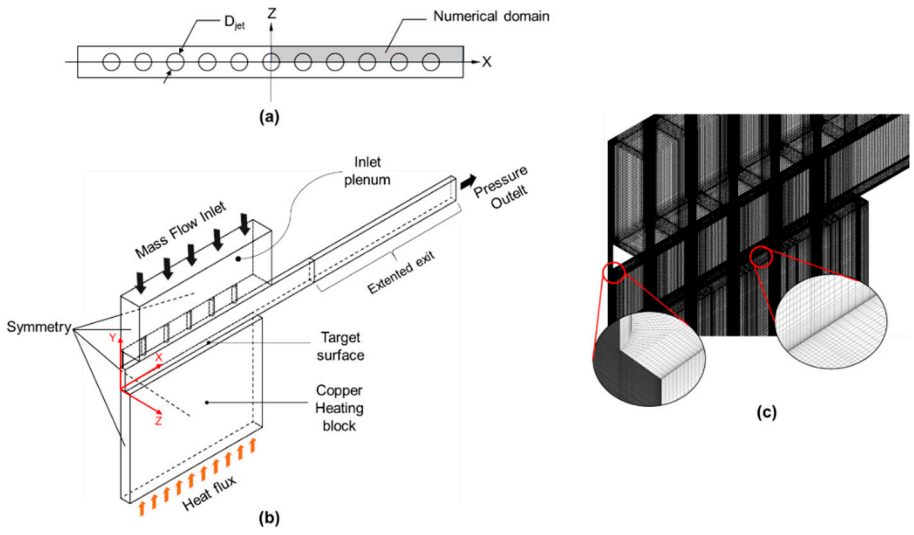

Figure 4. Numerical domain: (**a**) symmetry configuration; (**b**) boundary conditions; (**c**) grid system.

3.2. Numerical Method

The commercial computational fluid dynamics software, Ansys Fluent 20.1 [31], was used for the three-dimensional steady-state calculations. The Reynolds-averaged Navier–Stokes (RANS) approach using Menter's SST k-ω turbulence model was used to model the turbulent flow [32,33]. The SST k-ω model is a hybrid model that uses the k-ε turbulence model in the freestream and the k-ω turbulence model near the wall, where the blending function determines the smooth transition between the free stream and the flow near the wall. It was reported in previous studies that the SST k-ω turbulence model is suitable for turbulence modeling in jet impingement flows [17,34,35]. The governing equations are expressed as follows:

Continuity equation:

$$\frac{\partial(\rho U_j)}{\partial x_i} = 0 \tag{6}$$

Momentum equation:

$$\frac{\partial(\rho U_i U_j)}{\partial x_i} = -\frac{\partial P}{\partial x_i} + \frac{\partial}{\partial x_j}\left[(\mu + \mu_t)\left(\frac{\partial U_i}{\partial x_j} + \frac{\partial U_j}{\partial x_i}\right)\right] + \rho g_i \quad (7)$$

Energy equation:

$$\frac{\partial(\rho U_j c_p T)}{\partial x_j} = \frac{\partial}{\partial x_j}\left[\left(\lambda + \frac{c_p \mu_t}{Pr_t}\right)\frac{\partial T}{\partial x_j}\right] \quad (8)$$

The convergence was determined by checking both the residuals and the average heat transfer coefficient. When the residuals of continuity, momentum, and energy equations are less than 10^{-5}, and the average heat transfer coefficient at the target surface fluctuated less than 1%, the simulation was assumed to be converged, and the calculation was stopped. The SIMPLEC algorithm [36] was used for pressure–velocity coupling, and the second-order upwind scheme was used to discretize the flow variables. The numerical simulations were performed by a high-performance computer (16 processors, 112 parallel threads), and each of the numerical simulation cases took about 8 h.

3.3. Validation of Numerical Model

A grid independence test was conducted for five different grid systems for H_{ch} = 4 mm and V_{jet} = 9 m/s case, and the results are summarized in Table 3. The average heat transfer coefficients at the target surface were compared for each grid system, and the discrepancy was less than the experimental measurement error, 4%. Hence, the grid system with around 4.62 million elements was used for all the simulations.

Table 3. Grid independence test.

Number of Elements ($\times 10^6$)	Average Heat Transfer Coefficient (kW/m^2-K)
4.62	46.96
6.78	45.18
7.94	46.27
10.25	46.58
12.34	46.45

Experimentally measured and numerically calculated area-averaged Nusselt number (Nu_{avg}) values at V_{jet} = 2, 4, 6, 8 m/s for each channel height were compared to validate the numerical model. The heat flux and the mass flow rate measured in the experiments were applied as boundary conditions of the numerical domain. Figure 5 shows a comparison between numerically predicted Nu_{avg} and experimental measured Nu_{avg}. All the values are within a 10% error line, demonstrating that the numerical model can effectively simulate the channel impingement cooling configuration.

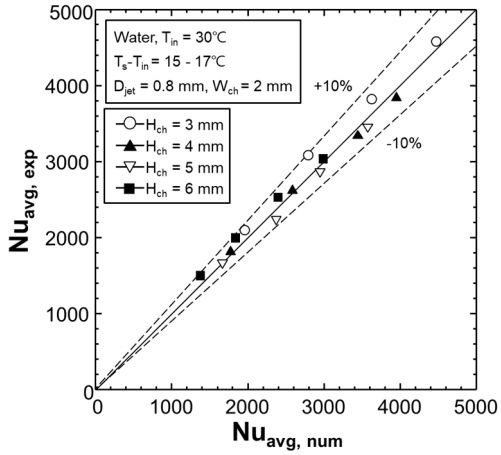

Figure 5. Comparison between experimentally measured and numerically calculated average Nusselt number.

4. Results and Discussion

4.1. Experimental Results

Figure 6a shows experimentally measured Nu_{avg} at the target surface for H_{ch} = 3, 4, 5, and 6 mm and Re_{jet} values ranging from 2000 to 8600. Nu_{avg} increases with Re_{jet}, indicating a power-law distribution. However, Nu_{avg} decreases with increasing H_{ch}. The detailed analysis of the H_{ch} and Re_{jet} effects on the flow structure and local heat transfer distribution is numerically investigated, and it will be discussed in detail in the following section. Data are correlated as a function of Re_{jet}, dimensionless channel height (H_{ch}/D_{jet}), and fluid properties evaluated at the jet exit temperature (k_f = 0.6194 W/m-K, $\mu_f = 7.773 \times 10^{-4}$ kg/m-s, ρ_f = 995 kg/m^3, Pr_f = 5.108).

$$Nu_{avg} = \frac{h_{avg} L_{ch}}{k_f} = 17.4\, Re_{jet}^{0.56} \left(\frac{H_{ch}}{D_{jet}}\right)^{-0.59} Pr_f^{0.33} \quad (9)$$

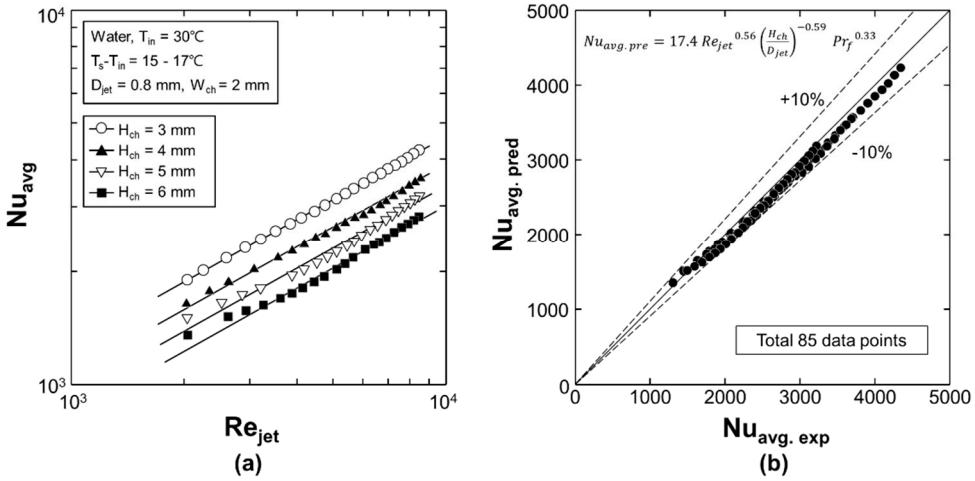

Figure 6. (**a**) Experimentally measured average Nusselt number; (**b**) comparison between experimentally measured average Nusselt number and new correlation.

Figure 6b compares the experimental and correlated Nu_{avg}. A total of 85 data points fall within the ±10% error lines with a mean absolute error of 4.31%.

4.2. Numerical Results

Numerical simulations are performed for different H_{ch}, V_{jet}, and q'' conditions listed in Table 4 to analyze the effects of channel height and mass flow rate on the flow field and heat transfer.

Table 4. H_{ch}, V_{jet}, and heat flux conditions for numerical analysis.

H_{ch} (mm)	V_{jet} (m/s)	q'' (W/cm^2)
3, 4, 5, 6	1	10
3, 4, 5, 6	5	18
3, 4, 5, 6	9	30

4.2.1. Jet Exit Velocity Variation

Considering uniform inlet plenum pressure and constant orifice hole discharge coefficient, repetitive fluid injections along the channel causes momentum acceleration and pressure drop, resulting in jet exit velocity variation [16,17]. Figure 7a shows the variation of jet exit mass velocity along the channel at different H_{ch}, where G_j is the jet exit mass velocity, and $\overline{G}_j$ is the averaged jet exit mass velocity. For H_{ch} = 3 mm and 6 mm, the difference between the minimum and maximum, $G_j/\overline{G}_j$, is 20.6% and 9.1%, respectively, because higher acceleration pressure drop occurs in the smaller channel due to higher crossflow velocity. Figure 7b depicts the streamwise $G_j/\overline{G}_j$ variation at H_{ch} = 6 mm for different V_{jet}. Although the effect of V_{jet} is relatively small than the effect of H_{ch}, the difference between the minimum and the maximum of $G_j/\overline{G}_j$ increases with V_{jet}. Similar trends are also identified for all the other H_{ch} conditions. Hence, the jet exit velocity variation is influenced by both H_{ch} and V_{jet}. However, the effect of H_{ch} is significant.

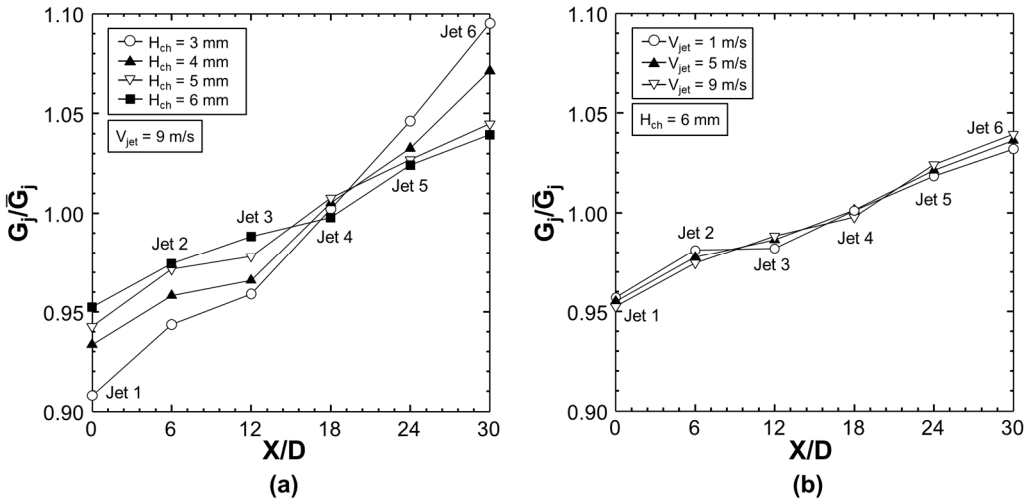

Figure 7. Variation of jet exit mass velocity at each jet holes: (**a**) V_{jet} = 9 m/s at H_{ch} = 3, 4, 5, and 6 mm; (**b**) H_{ch} = 6 mm at V_{jet} = 1, 5, and 9 m/s.

4.2.2. Flow Field and Heat Transfer Coefficient

Figure 8 displays the velocity contours at the middle of the channel (Z = 0 plane) and wall heat transfer coefficient at the target surface for V_{jet} = 1 m/s and different H_{ch}. The jet located at the center of the channel (X/D = 0) impinges on the target surface without deflection, yielding a local maximum heat transfer coefficient at the stagnation region. All the other jets get deflected by the crossflow. At all H_{ch}, the jet potential cores deflect in the streamwise direction. The farther the jet is from the center, the larger the deflections are due to accumulated crossflow. Deflected jets reach the target surface farther away from the jet hole position in the streamwise direction, which corresponds to the stagnation region and local high heat transfer regions in the heat transfer coefficient contours. The

deflected jets travel a longer distance to reach the target surface while interacting with crossflow. The jet travel distance to the target surface increases with the deflection. As a result, the deflected jets lose y-direction momentum, complicating the penetration of the thermal boundary layer formed on the target surface. Hence, the stagnation region heat transfer coefficient decreases at the downstream jet holes, except for the jet 2 stagnation heat transfer coefficient at H_{ch} = 3 mm (Figure 8a). For H_{ch} = 3 mm, the stagnation point heat transfer coefficient of jet 2 is higher than that of jet 1 due to the larger V_{jet} at jet 2, as shown in Figure 7a. As H_{ch} increases, the jet momentum loss increases, and the overall heat transfer coefficient decreases.

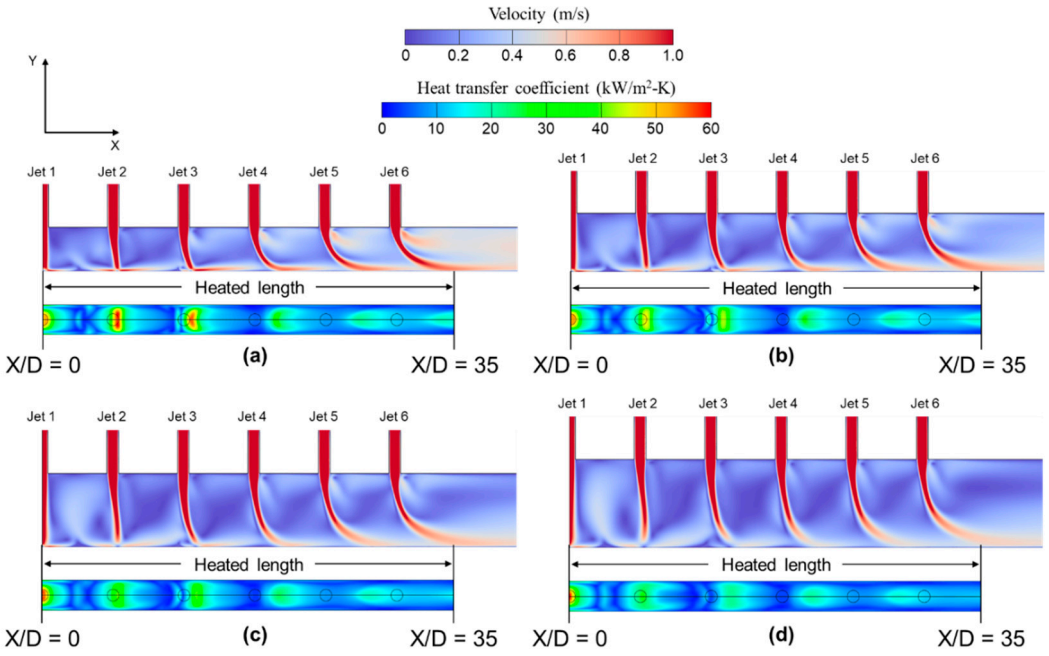

Figure 8. Velocity contours and wall heat transfer coefficient distributions at q'' = 10 W/cm^2 and V_{jet} = 1 m/s for (**a**) H_{ch} = 3 mm; (**b**) H_{ch} = 4 mm; (**c**) H_{ch} = 5 mm; (**d**) H_{ch} = 6 mm.

For V_{jet} = 5 m/s and 9 m/s, Figures 9 and 10 exhibit similar trends in both flow structure and heat transfer. Both Figures 9 and 10 demonstrate shifted stagnation points by jet deflection, degradation of heat transfer rate at the downstream jet, and lower heat transfer rate at higher H_{ch}, which are observed in Figure 8. For H_{ch} = 3 mm and 4 mm, Figures 9a,b and 10a,b shows that the heat transfer coefficient at the intervals between the stagnation regions increases with V_{jet} while maintaining local peaks at the stagnation regions. At high V_{jet}, when deflected jet impinges on the target surface, strong wall jet flow in streamwise direction covers the rear region of the stagnation points without detaching, which enhances heat transfer. For H_{ch} = 5 mm, Figures 9c and 10c show heat transfer enhancement at the intervals between the stagnation regions. However, heat transfer at the downstream stagnation region becomes weak because strong crossflow attached to the target surface hinders jet penetration, which is more evident at higher V_{jet} (See Figures 9c and 10c). For H_{ch} = 6 mm, velocity contours in Figures 9d and 10d evidence that the wall attached crossflow prevents the jet potential core from reaching the target surface, which causes the local peaks of the heat transfer coefficient at the stagnation regions to fade away.

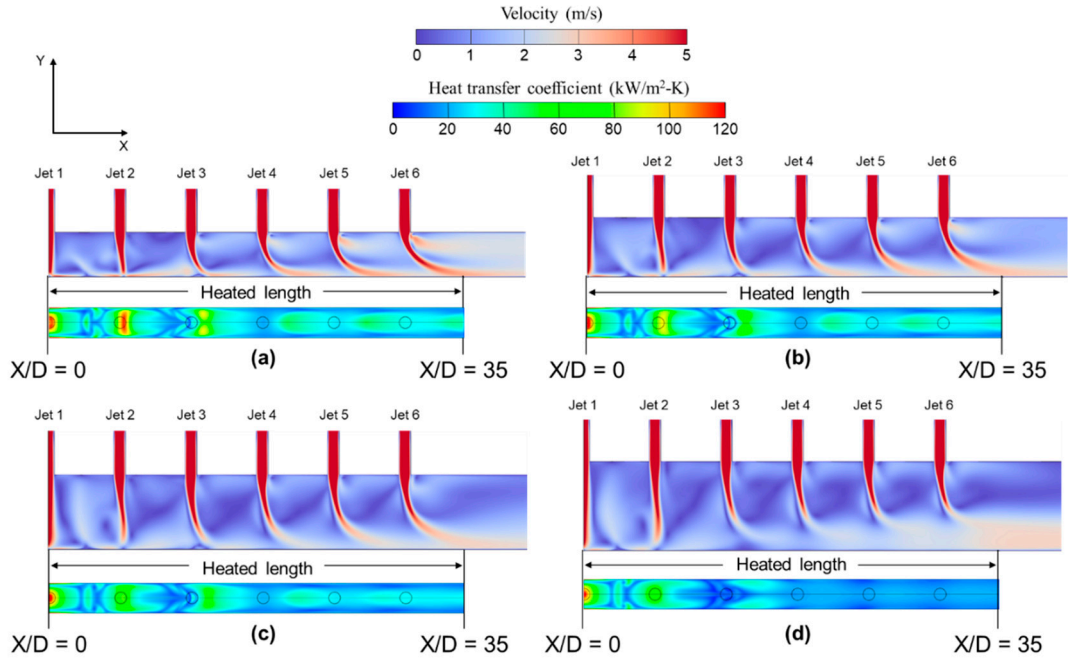

Figure 9. Velocity contours and wall heat transfer coefficient distributions at q'' = 18 W/cm^2 and V_{jet} = 5 m/s for (**a**) H_{ch} = 3 mm; (**b**) H_{ch} = 4 mm; (**c**) H_{ch} = 5 mm; (**d**) H_{ch} = 6 mm.

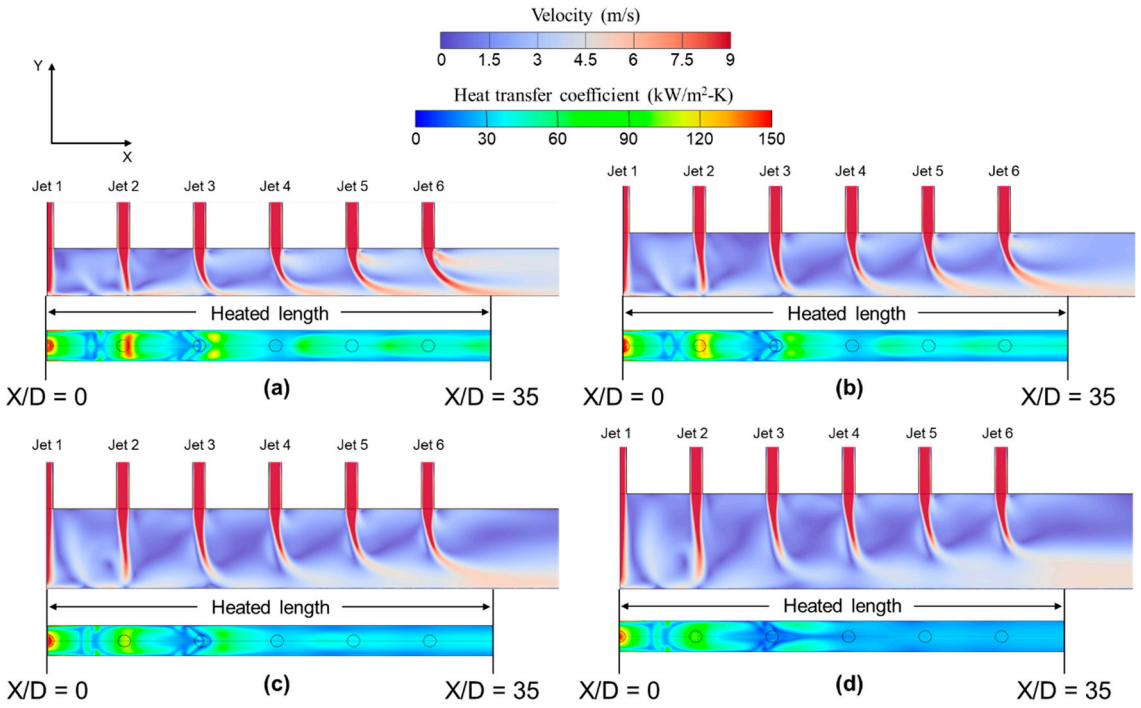

Figure 10. Velocity contours and wall heat transfer coefficient distributions at q'' = 30 W/cm^2 and V_{jet} = 9 m/s for (**a**) H_{ch} = 3 mm; (**b**) H_{ch} = 4 mm; (**c**) H_{ch} = 5 mm; (**d**) H_{ch} = 6 mm.

Figure 11 shows the velocity streamlines for H_{ch} = 4 mm and 6 mm at V_{jet} = 1 m/s and 9 m/s. For V_{jet} = 1 m/s and 9 m/s at H_{ch} = 4 mm, Figure 11a,b show similar flow structure resulting in similar heat transfer characteristics. For V_{jet} = 1 m/s at H_{ch} = 6 mm, Figure 11c shows that all the jets impinge on the target surface. However, for V_{jet} = 9 m/s at H_{ch} = 6 mm, Figure 11d evidences the inability of the jet to penetrate the crossflow since the thickness of the wall attached crossflow increases in the downstream direction. Velocity

vector distributions at both H_{ch} = 4 mm and 6 mm show a U-shaped clockwise rotating flow structure generated by the upstream jet and wall attached crossflow. The U-shaped clockwise rotating flow structure induces upward (+Y direction) flow near the downstream jet, which causes a detrimental effect on the downstream jet velocity evolution due to shear interaction. With increasing jet velocity, the strength of the rotating flow structure and the shear interaction increases regardless of H_{ch}, causing higher momentum loss.

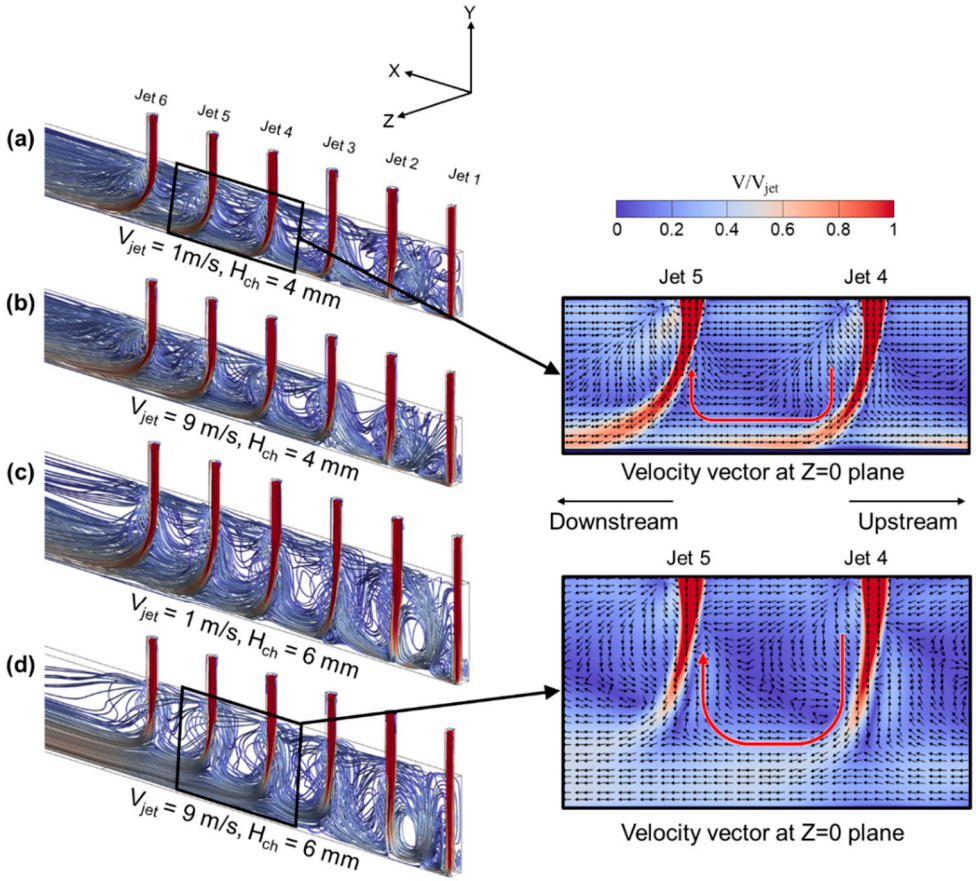

Figure 11. Velocity streamlines for (**a**) V_{jet} = 1 m/s, H_{ch} = 4 mm; (**b**) V_{jet} = 9 m/s, H_{ch} = 4 mm; (**c**) V_{jet} = 1 m/s, H_{ch} = 6 mm; (**d**) V_{jet} = 9 m/s, H_{ch} = 6 mm.

Figure 12 shows the spanwise (Z direction) averaged heat transfer coefficient along the streamwise direction (+X/D direction) for V_{jet} = 1, 5, and 9 m/s for each channel height at the target surface. The peaks at the location of stagnation regions decrease in the streamwise direction due to the jet momentum loss by the crossflow. The distinct peak regions are jet impingement flow dominant, and the region where the peaks flatten are channel flow dominant. Moreover, as previously discussed, the heat transfer coefficient decreases with an increase in H_{ch}.

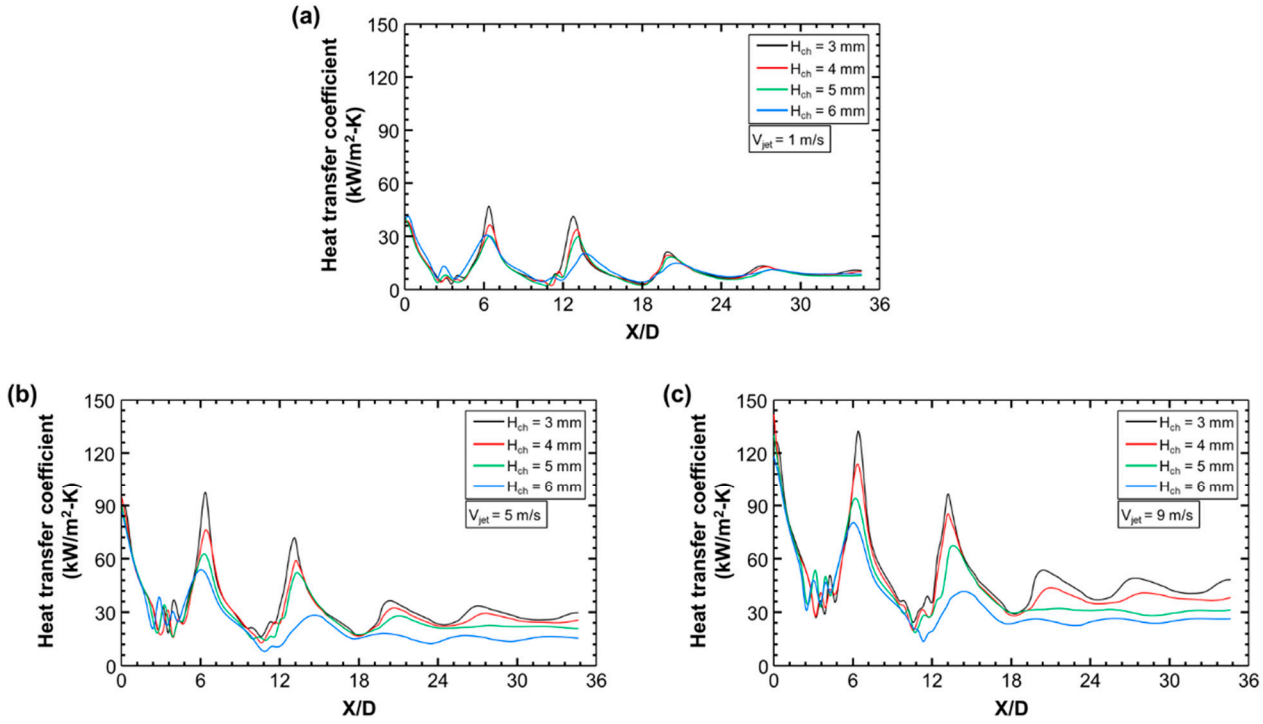

Figure 12. Spanwise averaged heat transfer coefficient distributions at target surface at (**a**) V_{jet} = 1 m/s; (**b**) V_{jet} = 5 m/s; (**c**) V_{jet} = 9 m/s.

5. Conclusions

The heat transfer and flow characteristics of channel impingement cooling with a single array of water jets were investigated experimentally and numerically. First, heat transfer coefficients at the target surface were measured for four different channel heights (H_{ch} = 3, 4, 5, and 6 mm) at jet Reynolds numbers within a range of 2000–8600. Then, numerical simulations were validated with the experimental results. Finally, the numerical results were analyzed for a deeper understanding of the flow field and its effect on local heat transfer characteristics. The key findings from the present study are as follows:

(1) Experimental results showed that the average Nusselt number (Nu_{avg}) at the target surface increases with the jet Reynolds number (Re_{jet}) and decreases with the channel height (H_{ch});

(2) Experimentally measured Nu_{avg} was correlated as a function of Re_{jet}, dimensionless channel height (H_{ch}/D_{jet}), and fluid properties. The correlated Nu_{avg} agreed well within a mean absolute error of 4.31%;

(3) The numerical simulation using the SST k-ω turbulence model can effectively predict experimentally measured overall heat transfer rate of the channel impingement configuration within a 10% error;

(4) Numerical results showed that a jet exit velocity variation occurs along the channel. The jet exit velocity variation was significantly affected by H_{ch} and moderately affected by the average jet velocity (V_{jet});

(5) The crossflow inside the channel deflects the jet potential core in the streamwise direction, and the stagnation regions occurred at the downstream location. The jet deflection reduced the stagnation region heat transfer, evident at the downstream located jets. The stagnation region heat transfer coefficient decreased with increasing channel height because the jet loses momentum traveling a long distance to the target surface;

(6) At high V_{jet}, a stronger wall jet covers the rear section of the stagnation region and the heat transfer at the intervals between stagnation regions increase. However, at high H_{ch}, the jet was unable to penetrate the wall attached crossflow at the downstream

location, and peaks in the heat transfer coefficient at the stagnation region faded away;

(7) U-shaped rotating flow structures formed by the wall attached crossflow and upstream jet were observed regardless of H_{ch} and V_{jet}. Shear interaction between the U-shaped flow structures and the downstream jet caused a detrimental effect on the velocity evolution and induced jet momentum loss.

Author Contributions: Validation, methodology, software, investigation, writing—original draft, M.-S.S.; validation, writing—original draft, S.S.; conceptualization, methodology, supervision, writing—review and editing, S.-M.K. All authors have read and agreed to the published version of the manuscript.

Funding: This work was supported by the Technology Innovation Program (20013794, Center for Composite Materials and Concurrent Design), funded by the Ministry of Trade, Industry & Energy (MOTIE, Korea).

Conflicts of Interest: The authors declare no conflict of interest.

References

1. Harms, T.M.; Kazmierczak, M.J.; Gerner, F.M. Developing convective heat transfer in deep rectangular micro-channels. *Int. J. Heat Fluid Flow* **1999**, *20*, 149–157. [CrossRef]
2. Qu, W.; Mudawar, I. Experimental and numerical study of pressure drop and heat transfer in a single-phase micro-channel heat sink. *Int. J. Heat Mass Transf.* **2002**, *45*, 2549–2565. [CrossRef]
3. Memon, S.A.; Cheema, T.A.; Kim, G.M.; Park, C.W. Hydrothermal investigation of a microchannel heat sink using secondary flows in trapezoidal and parallel orientations. *Energies* **2020**, *13*, 5616. [CrossRef]
4. Zhang, Y.-D.; Chen, M.-R.; Wu, J.-H.; Hung, K.-S.; Wang, C.-C. Performance improvement of a double-layer microchannel heat sink via novel fin geometry—A numerical study. *Energies* **2021**, *14*, 3585. [CrossRef]
5. Rybicki, J.R.; Mudawar, I. Single-phase and two-phase cooling characteristics of upward-facing and downward-facing sprays. *Int. J. Heat Mass Transf.* **2006**, *49*, 5–16. [CrossRef]
6. Estes, K.A.; Mudawar, I. Correlation of Sauter mean diameter and critical heat flux for spray cooling of small surfaces. *Int. J. Heat Mass Transf.* **1995**, *38*, 2985–2996. [CrossRef]
7. Natarajan, G.; Bezama, R.J. Microjet cooler with distributed returns. *Heat Transf. Eng.* **2007**, *28*, 779–787. [CrossRef]
8. Rattner, A.S. General characterization of jet impingement array heat sinks with interspersed fluid extraction ports for uniform high-flux cooling. *J. Heat Transf.* **2017**, *139*, 082201. [CrossRef]
9. Paniagua-Guerra, L.E.; Sehgal, S.; Gonzalez-Valle, C.U.; Ramos-Alvarado, B. Fractal channel manifolds for microjet liquid cooled heat sinks. *Int. J. Heat Mass Transf.* **2019**, *138*, 257–266. [CrossRef]
10. Wu, R.; Fan, Y.; Hong, T.; Zou, H.; Hu, R.; Luo, X. An immersed jet array impingement cooling device with distributed returns for direct body liquid cooling of high power electronics. *Appl. Ther. Eng.* **2019**, *162*, 114259. [CrossRef]
11. Xing, Y.; Spring, S.; Weigand, B. Experimental and numerical investigation of heat transfer characteristics of inline and staggered arrays of impinging jets. *J. Heat Transf. Trans. ASME* **2010**, *132*. [CrossRef]
12. Hollworth, B.R.; Lehmann, G.; Rosiczkowski, J. Arrays of impinging jets with spent fluid removal through vent holes on the target surface, Part 2: Local heat transfer. *J. Eng. Power Trans. ASME* **1983**, *105*, 393–402. [CrossRef]
13. Huber, A.M.; Viskanta, R. Effect of jet-jet spacing on convective heat transfer to confined, impinging arrays of axisymmetric air jets. *Int. J. Heat Mass Transf.* **1994**, *37*, 2859–2869. [CrossRef]
14. Cho, H.H.; Rhee, D.H. Local heat/mass transfer measurement on the effusion plate in impingement/effusion cooling system. *J. Turbomach. Trans. ASME* **2001**, *123*, 601–608. [CrossRef]
15. Hoberg, T.B.; Onstad, A.J.; Eaton, J.K. Heat transfer measurement for jet impingement arrays with local extraction. *Int. J. Heat Fluid Flow* **2010**, *31*, 460–467. [CrossRef]
16. Ricklick, M.; Kapat, J.S.; Heidmann, J. Sidewall effects on heat transfer coefficient in a narrow impingement channel. *J. Theromphys. Heat Transf.* **2010**, *24*, 123–132. [CrossRef]
17. Fechter, S.; Terzis, A.; Ott, P.; Weigand, B.; von Wolfersdorf, J.; Cochet, M. Experimental and numerical investigation of narrow impingement cooling channels. *Int. J. Heat Mass Transfer.* **2013**, *67*, 1208–1219. [CrossRef]
18. Terzis, A.; Ott, P.; von Wolfersdorf, J.; Weigand, B.; Cochet, M. Detailed heat transfer distribution of narrow impingement channels for cast-in turbine airfoils. *ASME J. Turbomach.* **2014**, *136*, 091011. [CrossRef]
19. Hossain, J.; Tran, L.V.; Kapat, J.S.; Fernandez, E.; Kumar, R. An experimental study of detailed flow and heat transfer analysis in a single row narrow impingement channel. In Proceedings of the Turbo Expo 2014: Turbine Technical Conference and Exposition, Düsseldorf, Germany, 16–20 June 2014.
20. Zhang, J.; Sun, Y.; Li, J.; He, X. Study on the hybrid cooling of the flame tube in a small triple-swirler combustor. *Energies* **2020**, *13*, 5554. [CrossRef]
21. Agrawal, C.; Kumar, R.; Gupta, A.; Chatterjee, B. Rewetting and maximum surface heat flux during quenching of hot surface by round water jet impingement. *Int. J. Heat Mass Transf.* **2012**, *55*, 4772–4782. [CrossRef]

22. Johns, M.E.; Mudawar, I. An ultra-high power two-phase jet impingement avionic clamshell module. *ASME.J. Electron. Packag.* **1996**, *118*, 264–270. [CrossRef]
23. Narumanchi, S.V.J.; Hassani, V.; Bharathan, D. *Modeling Single-Phase and Boiling Liquid Jet Impingement Cooling in Power Electronics*; National Renewable Energy Laboratory (NREL): Golden, CO, USA, 2005.
24. Obot, N.T.; Trabold, T.A. Impingement heat transfer within arrays of circular jets: Part 1-Effects of minimum, intermediate, and complete crossflow for small and large spacings. *J. Heat Transf. Trans. ASME* **1987**, *109*, 872–879. [CrossRef]
25. Huang, Y.; Ekkad, S.V.; Han, J.C. Detailed heat transfer distributions under an array of orthogonal impinging jets. *J. Thermophys. Heat Transf.* **1998**, *12*, 73–79. [CrossRef]
26. Miao, J.M.; Wu, C.Y.; Chen, P.H. Numerical investigation of confined multiple-jet impingement cooling over a flat plate at different crossflow orientaions. *Numer. Heat Transf. Part A Appl.* **2009**, *55*, 1019–1050. [CrossRef]
27. Sung, M.K.; Mudawar, I. Single-phase hybrid micro-channel/micro-jet impingement cooling. *Int. J. Heat Mass Transf.* **2008**, *51*, 4342–4352. [CrossRef]
28. Sung, M.K.; Mudawar, I. Effects of jet pattern on single-phase cooling performance of hybrid micro-channel/micro-circular-jet-impingement thermal management scheme. *Int. J. Heat Mass Transf.* **2008**, *51*, 4614–4627. [CrossRef]
29. Barrau, J.; Chemisana, D.; Rosell, J.; Tadrist, L.; Ibanez, M. An experimental study of a new hybrid jet impingement/micro-channel cooling scheme. *Appl. Ther. Eng.* **2010**, *30*, 2058–2066. [CrossRef]
30. Barrau, J.; Omri, M.; Chemisana, D.; Rosell, J.; Ibanez, M.; Tadrist, L. Numerical study of a hybrid jet impingement/micro-channel cooling scheme. *Appl. Ther. Eng.* **2012**, *33–34*, 237–245. [CrossRef]
31. Ansys Fluent 20.1. *Theory Guide 2019*; ANSYS, Inc.: Canonsburg, PA, USA, 2019.
32. Menter, F.R. Zonal two equation k-ω turbulence models for aerodynamic flows. In Proceedings of the 24th Fluid Dynamics Conference, Orlando, FL, USA, 6–9 July 1993.
33. Menter, F.R. Two-equation eddy-viscosity turbulence models for engineering applications. *AIAA J.* **1994**, *32*, 1598–1605. [CrossRef]
34. Alimohammadi, S.; Murray, D.B.; Persoons, T. Experimental validation of a computational fluid dynamics methodology for transitional flow heat transfer characteristics of a steady impinging jet. *J. Heat Transf.* **2014**, *136*, 091703. [CrossRef]
35. Zuckerman, N.; Lior, N. Jet impingement heat transfer: Physics, correlations, and numerical modeling. *Adv. Heat Transf.* **2006**, *39*, 565–631.
36. Van Doormaal, J.P.; Raithby, G.D. Enhancements of the simple method for predicting incompressible fluid flows. *Numer. Heat Transf.* **1984**, *11*, 147–163.